

Speckle-correlation imaging through a kaleidoscopic multimode fiber

Dorian Bouchet,^{1,*} Antonio M. Caravaca-Aguirre,¹ Philippe Moreau,¹ Irène Wang,¹ and Emmanuel Bossy¹

¹Université Grenoble Alpes, CNRS, LIPhy, 38000 Grenoble, France

Speckle-correlation imaging techniques are widely used for non-invasive imaging through complex scattering media. While light propagation through multimode fibers and scattering media share many analogies, reconstructing images through multimode fibers from speckle correlations remains an unsolved challenge. Here, we exploit a kaleidoscopic memory effect emerging in square-core multimode fibers and demonstrate fluorescence imaging with no prior knowledge on the fiber. Experimentally, our approach simply requires to translate random speckle patterns at the input of a square-core fiber and to measure the resulting fluorescence intensity with a bucket detector. The image of the fluorescent object is then reconstructed from the autocorrelation of the measured signal by solving an inverse problem. This strategy does not require the knowledge of the fragile deterministic relation between input and output fields, which makes it promising for the development of robust minimally-invasive endoscopes.

The development of optical endoscopes is motivated by a number of biomedical applications such as brain imaging [1]. Multimode fibers are excellent candidates to minimize the invasiveness of such procedures, as they feature a high density of modes per unit area [2, 3]. However, coherent light propagating inside such fibers typically generates speckle patterns at the fiber output, in a similar way as through complex scattering media [4]. Different methods have emerged to exploit the complex deterministic relation between incident and transmitted fields in multimode fibers, based on either experimental measurements [5–11] or theoretical modeling [12, 13]. Nevertheless, these methods require either an optical access to both sides of the fiber or a precise knowledge of the fiber geometry over its entire length, which makes them unsuitable for many applications.

In contrast, statistical approaches based on speckle correlations can be implemented without such prior information. In the last decade, these strategies have been successfully employed to image fluorescent objects through layers of scattering materials [14–18]. A key component of these approaches is the existence of a memory effect, which creates statistical correlations between incident and transmitted fields [19–24]. However, multimode fibers have different statistical properties as compared to scattering materials [25–27]. A rotational memory effect exists in commonly-used circular-core multimode fibers [25], but it must be completed by additional information (using e.g. a fluorescent guidestar) in order to form an image [27]. Recently, deep neural networks have emerged as promising tools to learn not only deterministic but also statistical relations in multimode fibers [28–31], but with a generalizability limited to the specific experimental conditions under which the training dataset was measured. Thus, most practical implementations of fiber-optic endoscopes remain currently based on multicore fibers [32–34], which are characterized by a much larger footprint as compared to multimode fibers.

Traditionally in optical fibers, the geometry of the core is circular, and the use of square-core fibers is limited to specific applications requiring a top-hat-like intensity profile [35]. However, it was recently observed that a kaleidoscopic memory effect emerges from the strong symmetry properties of square-core multimode fibers [36]. This effect is a special type of shift-shift correlation [23]: any pattern translating at the fiber input leads to speckle patterns shifting along four directions at the output. The memory effect thus spans the whole two-dimensional (2D) space in square-core fibers, as opposed to conventional multimode fibers with a circular core geometry for which there exists no true radially-shifting memory effect [25, 27]. Taking advantage of the kaleidoscopic memory effect in square-core fibers, we present here a fully-statistical method to perform endoscopic imaging from speckle correlations, without relying on transmission matrix measurements or on fluorescent guidestars.

The principle of the proposed approach is illustrated in Fig. 1 (see also Methods for a detailed description of the experimental setup). A fluorescent sample is placed at the output of a step-index square-core optical fiber (CeramOptec, core section $100\text{ }\mu\text{m} \times 100\text{ }\mu\text{m}$, length 30 mm). In our proof-of-principle experiment, this sample is composed of several fluorescent beads (ThermoFisher Scientific, red FluoSpheres, diameter $1.0\text{ }\mu\text{m}$). We generate random speckle patterns at the fiber input using a digital micromirror device (DMD), and the transmitted light forms unknown speckle patterns that excite the fluorescent beads. Fluorescence collected through the fiber is then measured by a bucket detector located at the fiber input.

In order to exploit shift-shift correlations in the fiber, we translate the incident field in the transverse plane by $\mathbf{r}_a = (x_a, y_a)$ and we measure the resulting fluorescence signal $S(\mathbf{r}_a)$, with a scan area of $8\text{ }\mu\text{m} \times 8\text{ }\mu\text{m}$. While this signal visually appears as being random, it does carry useful information about the hidden fluorescent object. More precisely, the density distribution of fluorescent emitters $O(\mathbf{r}_b)$ is related to the measured fluorescence

* dorian.bouchet@univ-grenoble-alpes.fr

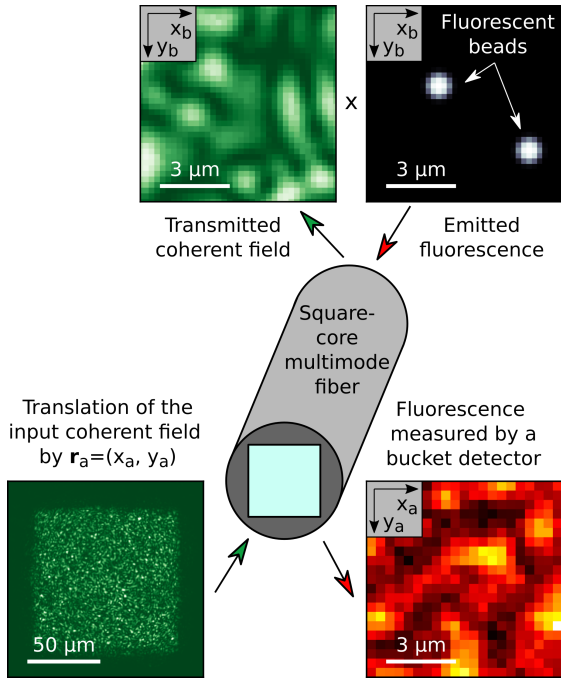


FIG. 1. Principle of a minimally-invasive endoscope based on a square-core multimode fiber. Coherent speckle patterns are translated in the transverse plane at the input of a square-core multimode fiber. Transmitted intensity patterns, which are unknown, excite a fluorescent sample located at the output of the fiber. Fluorescence is collected by the same fiber and is subsequently measured by a bucket detector located at the fiber input. Our method enables one to reconstruct an image of the sample from the seemingly-random fluorescence signal measured as a function of the translation \mathbf{r}_a of the input field.

signal $S(\mathbf{r}_a)$ by the following relation:

$$S(\mathbf{r}_a) = \int O(\mathbf{r}_b) I(\mathbf{r}_a, \mathbf{r}_b) d\mathbf{r}_b , \quad (1)$$

where $I(\mathbf{r}_a, \mathbf{r}_b)$ is the (unknown) excitation intensity transmitted at a position \mathbf{r}_b at the fiber output for a translation \mathbf{r}_a of the speckle pattern at the fiber input. From Eq. (1), we demonstrate in Supplementary Section 2 that the normalized autocorrelation function of the measured fluorescence signal is expressed as follows (see also Fig. 2 for a graphical interpretation of this equation):

$$C_S(\Delta\mathbf{r}_a) = K^{-2} \int C_O(\Delta\mathbf{r}_b) C_I(\Delta\mathbf{r}_a, \Delta\mathbf{r}_b) d\Delta\mathbf{r}_b , \quad (2)$$

where $C_O(\Delta\mathbf{r}_b)$ is the autocorrelation of the fluorescent object, $C_I(\Delta\mathbf{r}_a, \Delta\mathbf{r}_b)$ is the (known) intensity correlation function of the transmitted excitation intensity, and K is a normalization constant equal to the contrast of the fluorescence signal.

Equation (2), which does not directly involve the object but its autocorrelation (see Fig. 2b,c), is formally

identical to the one describing how to image fluorescent objects through scattering layers [14]. However, while the intensity correlation function C_I describing light propagation through scattering layers is characterized by a single peak arising from the usual memory effect [19, 20], the symmetry of the fiber generates a kaleidoscopic memory effect characterized by a different intensity correlation function [36]. Indeed, C_I is then characterized by four peaks that translate with $\Delta\mathbf{r}_a$ and that coherently overlap by pair when $\Delta x_a = 0$ or $\Delta y_a = 0$ (see Fig. 2d-g). As a consequence, the autocorrelation of the measured fluorescence signal does not directly yield the object autocorrelation. Instead, it involves $C_O^{\text{sym}}(\Delta\mathbf{r}_b) = [C_O(\Delta x_b, \Delta y_b) + C_O(\Delta x_b, -\Delta y_b)]/2$, which is a symmetrized version of the object autocorrelation (see Fig. 2h). Note that this expression is indeed centrosymmetric: since C_O is an even function of $\Delta\mathbf{r}_b$, we can write $C_O(\Delta x_b, \Delta y_b) = C_O(-\Delta x_b, -\Delta y_b)$ and $C_O(\Delta x_b, -\Delta y_b) = C_O(-\Delta x_b, \Delta y_b)$.

In order to understand how the signal autocorrelation C_S relates to the symmetrized object autocorrelation C_O^{sym} , it is instructive to first consider the limiting case of an infinite-range memory effect with a speckle grain size approaching zero. In this case, Eq. (2) yields $C_S(\Delta\mathbf{r}_a) \propto w(\Delta\mathbf{r}_a) C_O^{\text{sym}}(\Delta\mathbf{r}_a)$, where w is a weight function that is equal to 1 if $\Delta x_a = 0$ and $\Delta y_a = 0$, to 1/2 if either $\Delta x_a = 0$ or $\Delta y_a = 0$, and to 1/4 otherwise (see Supplementary Section 3). In practice, the translational memory effect observed in typical step-index square-core optical fibers is further characterized by a limited range [36], and the measured intensity correlation $C_I(\Delta\mathbf{r}_a, \Delta\mathbf{r}_b)$ gradually decays with the distance $\Delta\mathbf{r}_a$. As a consequence, the signal autocorrelation $C_S(\Delta\mathbf{r}_a)$ predicted from Eq. (2) also decays with $\Delta\mathbf{r}_a$ (see Fig. 2i), limiting the potential reconstruction area to approximately $10 \mu\text{m} \times 10 \mu\text{m}$ for the type of step-index fiber used in our experiment. In addition, the finite size of the speckle grain limits the achievable resolution of the method, which is of approximately $1.2 \mu\text{m}$ in our experiment (excitation wavelength $\lambda = 532 \text{ nm}$, fiber numerical aperture NA = 0.22).

Reconstructing fluorescent objects from measurements of the signal autocorrelation C_S thus amounts to retrieve O from C_O^{sym} . This inverse problem has no known explicit solution, but it can be solved iteratively by exploiting additional prior knowledge about the object as constraints. This problem is in fact deeply connected to commonly-encountered phase-retrieval problems [37, 38], and especially to autocorrelation inversions [14]. It essentially differs from such problems in two aspects. First, as the intensity correlation function $C_I(\Delta\mathbf{r}_a, \Delta\mathbf{r}_b)$ is characterized by four peaks instead of one, there exists an additional ambiguity in the inverse problem to be solved. Indeed, for a given fluorescent object, there exists four equivalent solutions that are flipped versions of the object (see Supplementary Section 4), instead of two in typical autocorrelation inversions. Second, the signal autocorrelation is weighted by a factor of 1/4 (instead of 1) when

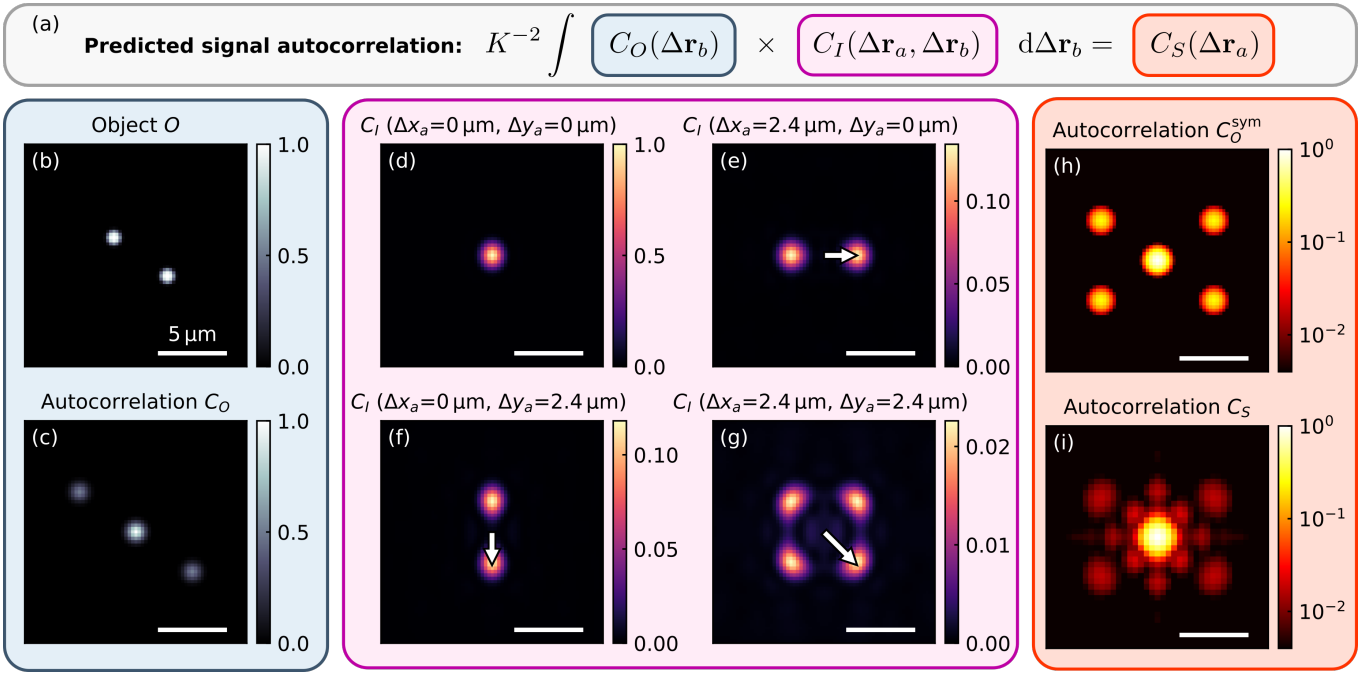


FIG. 2. Predicted autocorrelation of the fluorescence signal. (a) Graphical representation of Eq. (2) relating the object autocorrelation $C_O(\Delta \mathbf{r}_b)$, the intensity correlation function of the excitation field $C_I(\Delta \mathbf{r}_a, \Delta \mathbf{r}_b)$ and the autocorrelation of the fluorescence signal $C_S(\Delta \mathbf{r}_a)$. (b) Fluorescent object $O(\mathbf{r}_b)$ composed of two beads (diameter, $1.0 \mu\text{m}$), that we model here using high-order Gaussian functions. (c) Object autocorrelation $C_O(\Delta \mathbf{r}_b)$ calculated from $O(\mathbf{r}_b)$. (d-g), Intensity correlation function of the excitation field $C_I(\Delta \mathbf{r}_a, \Delta \mathbf{r}_b)$, represented as a function of $\Delta \mathbf{r}_b$ (shift at the fiber output) for four different values of $\Delta \mathbf{r}_a$ (shift at the fiber input). This correlation function, which characterizes light propagation in square-core multimode fibers, is composed of four peaks that translate when changing the value of $\Delta \mathbf{r}_a$ (white arrows on the figures). (h) Symmetrized autocorrelation of the object $C_O^{\text{sym}}(\Delta \mathbf{r}_b)$. (i) Predicted signal autocorrelation $C_S(\Delta \mathbf{r}_a)$ calculated using Eq. (2). The 4 main lobes that appear in $C_O^{\text{sym}}(\Delta \mathbf{r}_b)$ are also identified in $C_S(\Delta \mathbf{r}_a)$, but with a smaller amplitude due to the finite range of the memory effect. A number of additional lobes can be identified close to the central peak, due to the presence of lobes in the intensity correlation function $C_I(\Delta \mathbf{r}_a, \Delta \mathbf{r}_b)$.

$\Delta x_a \neq 0$ and $\Delta y_a \neq 0$. This effect, when cumulated to the continuous decay of the correlation function with $\Delta \mathbf{r}_a$, increases the influence of the statistical fluctuations that are observed when estimating correlation functions from experimental measurements. In practice, to counteract this effect, we generate and translate random incident fields at kilohertz frequencies using the DMD; this allows us to average the signal correlation function over many random configurations of the input speckle, thereby preventing the apparition of artifacts due to statistical fluctuations.

We experimentally illustrate this approach on three different fluorescent objects composed of 2, 3 and 4 beads, respectively (Fig. 3a,e,i). The predicted signal autocorrelation function (Fig. 3b,f,j), calculated using Eq. (2), strongly depends on the object, which explicitly demonstrates that this function does carry spatial information about the object. Moreover, autocorrelation functions retrieved from experimental measurements (Fig. 3c,g,k) are in excellent agreement with theoretically-predicted ones. These results were obtained by averaging over $N_{\text{rep}} = 40,000$ realizations of input speckles; while reduc-

ing N_{rep} inevitably leads to the apparition of artifacts due to statistical fluctuations, some spatial information about the fluorescent objects is still present even for much lower values of N_{rep} (see Supplementary Section 5). Based on these experimental data and on the forward model expressed by Eq. (2), we could in principle reconstruct an image using a pixel-by-pixel approach. However, the inverse problem is more easily solved when using additional *a priori* information about the object. Here, we take advantage of known characteristics of the beads, setting a bead diameter of $1 \mu\text{m}$ and assuming that all beads have the same brightness. We then estimate the number of fluorescent beads using the statistics of the measured signal (see Supplementary Section 6). Finally, we use an optimization algorithm based on simulated annealing [39] in order to find the beads positions that minimize the error between theoretical predictions and experimental data (see Supplementary Section 7). The reconstructed images (Fig. 3d,h,l) are in excellent agreement with direct images of the objects (i.e. the ground truths), demonstrating that, even though light is apparently scrambled when propagating through square-core multimode fibers,

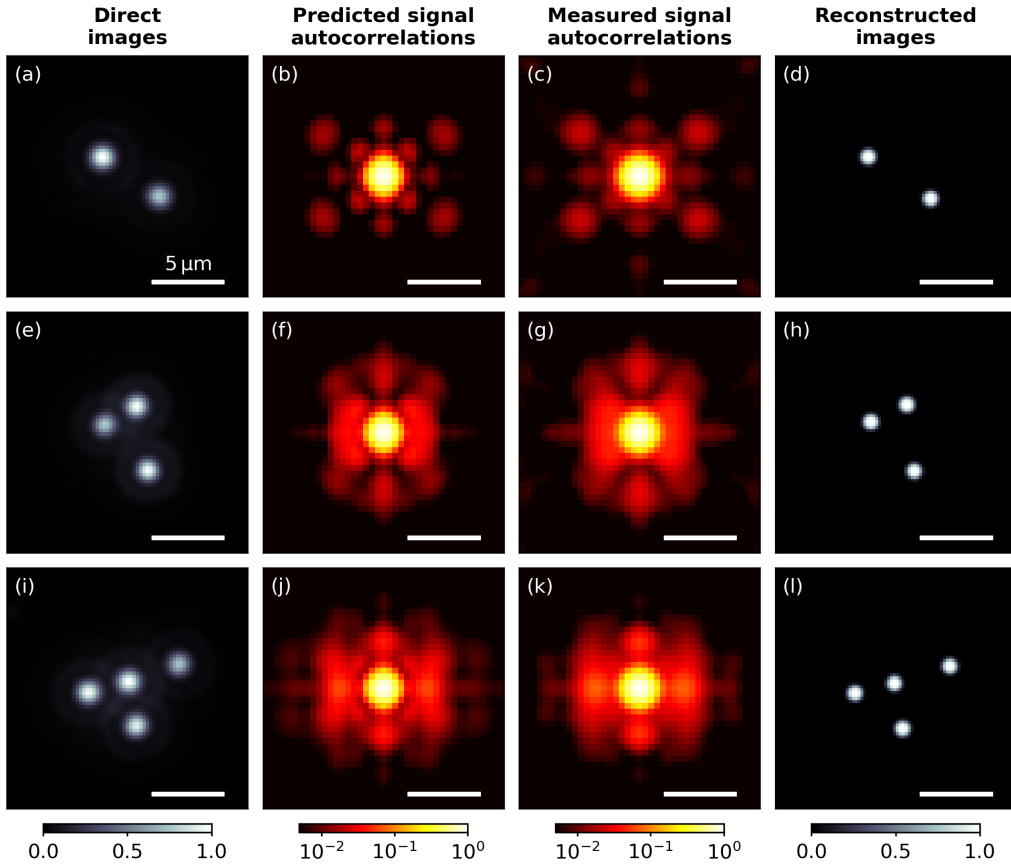


FIG. 3. Reconstructed images of fluorescent beads from experimental measurements. (a) Direct fluorescence image of a sample composed of two beads. (b) Predicted signal autocorrelation calculated with the true beads positions using Eq. (2). (c) Signal autocorrelation retrieved from experimental measurements (averaged over $N_{\text{rep}} = 40,000$ speckle illuminations). (d) Reconstructed image of the beads. The number of beads is first estimated independently from the statistics of the measured signal, and the beads position is then retrieved using an optimization algorithm based on simulated annealing. (d-l) Analogous to (a-d) for objects composed of three beads (e-h) and four beads (i-l).

2D spatial information about fluorescent samples can be effectively recovered with a fully-statistical imaging strategy.

To conclude, we introduced an approach to reconstruct images through a multimode optical fiber based on speckle correlations, without any prior information on the fiber. This approach takes advantage of symmetries in square-core fibers, which induce a kaleidoscopic memory effect that can be exploited to reconstruct images through the fiber. As an illustration, we reconstructed images of samples composed of several fluorescent beads, as being relevant e.g. for applications involving fluorescent emitters as functional indicators [40, 41]. Imaging more complex fluorescent objects could be achieved by extending the field of view of the method and by improving the reconstruction algorithm used to solve the inverse problem. A possible way to extend the field of view consists in optimizing the optical properties of the fiber, so that boundary conditions at the core-cladding interface are closer to those of a perfect mirror. Furthermore, we anticipate that more efficient strategies to solve the inverse problem

will emerge from the recently-established fields of compressed sensing [42] and artificial intelligence [43], e.g. by reducing the influence of statistical fluctuations and by finding adequate sparsity constraints. Finally, we highlight that our method is generally applicable not only to fluorescent objects but also to any sample that generates a signal in response to light, such as photo-acoustic emission from optical absorbers [44–46] or second-harmonic generation from non-linear materials [47, 48].

METHODS

Sample preparation Fluorescent objects are composed of latex microspheres (ThermoFisher Scientific, red FluoSpheres, diameter 1.0 μm) dispersed on a glass coverslip. A solution of Poly-L-lysine (Sigma-Aldrich, 0.1 % in H_2O) is first deposited on a clean coverslip in order to fix the microspheres. A solution of fluorescent beads diluted in water is then deposited on the coverslip. Using this procedure, fluorescent beads are randomly dispersed

on the sample. In order to detect only the fluorescence of the few beads of interest, we selectively photobleach all other beads within the field of view of the fiber (area of $100\text{ }\mu\text{m} \times 100\text{ }\mu\text{m}$) by successively focusing coherent light from a continuous-wave laser (Cobolt 08-DPL, 532 nm, 10 mW after attenuation by a neutral density filter) on the beads using a $\times 20$ objective (Mitutoyo Plan Apo SL 20X/0.28).

Optical setup The optical setup that we built to image fluorescent samples through a multimode fiber is represented in Supplementary Section 1. Coherent light is generated by a continuous-wave solid-state laser (Cobolt 08-DPL, 532 nm). Light is injected in a single-mode polarization-maintaining fiber and outcoupled using a collimator (Schäfter+Kirchhoff 60FC-L-4-M75-01). Light then passes through a linear polarizer to ensure that it is horizontally polarized, before being reflected by a digital micromirror device (Vialux Superspeed V-7001). Random speckle patterns are generated and translated in the plane of the fiber using Lee holography [49]. This technique is implemented using a 4f system composed of a 300 mm lens (L1) and a 150 mm lens (L2). In the focal plane between these lenses, an iris selects the first diffraction order of the grating displayed by the DMD. A dichroic mirror (Chroma ZT532rdc) reflects the light towards a $\times 20$ objective (Nikon CF Plan 20X/0.35 EPI SLWD), and a square-core multimode fiber (CeramOptec, core section $100\text{ }\mu\text{m} \times 100\text{ }\mu\text{m}$, cladding diameter $123\text{ }\mu\text{m}$, length 30 mm, numerical aperture 0.22) is placed in its focal plane. The input speckle patterns generated using this procedure are characterized by a numerical aperture of 0.22 (to match that of the fiber) and a spatial extent of $92\text{ }\mu\text{m} \times 92\text{ }\mu\text{m}$. This allows us to translate the patterns over an area of $8\text{ }\mu\text{m} \times 8\text{ }\mu\text{m}$ without illuminating the fiber cladding. Note that, to avoid auto-fluorescence of the fiber coating, we removed it using a solution of trichloromethane.

The sample, located approximately $20\text{ }\mu\text{m}$ away from the fiber output, is thus illuminated by light coming from the fiber. Fluorescence light is then collected by the same fiber and, after passing through the dichroic mirror, it is spatially filtered using a 4f system composed of a 200 mm lens (L3) and a 100 mm lens (L4), with an iris located in the focal plane in-between these lenses. This iris is used to block unwanted light coming from outside of the fiber core. Light is then spectrally filtered using two successive fluorescence filters (Thorlabs NF533-17 and Chroma ET577LP) and focused using a 150 mm lens onto a photomultiplier tube module (Hammamatsu H7422P). The

measured analog signal passes a low-noise current amplifier (Stanford Research Systems SR570), which applies a low-pass filter to the signal (-6 dB cutoff frequency: 10 kHz) in order to improve the signal-to-noise ratio. Finally, this analog signal is converted into a digital signal by an acquisition board (National Instruments PCIe-6321).

Acquisition procedure To minimize the acquisition time, we first pre-calculate the patterns that will be displayed by the DMD. These patterns are splitted into packets of 79 realizations of input speckles, each of them containing 21×21 patterns which are translated versions of the same speckle. These files are then stored on a solid-state drive (SSD) in a binary format. During an acquisition, each file is loaded on the random access memory (RAM) of the computer (loading time, 2.4 s), then transferred into the internal memory of the DMD (transfer time, 8.7 s), and finally displayed by the DMD running at a rate of 2 kHz (display time, 17.4 s). While our DMD could be operated at a rate of up to 23 kHz, working at 2 kHz allows us to improve the signal-to-noise ratio by applying a low-pass filter (-6 dB cutoff frequency: 10 kHz) to the measured signal. Overall, measuring data for 40,000 realizations takes 4 hours; nevertheless, the quality of reconstructed images is already relatively good with 3,000 realizations (see Supplementary Section S5), that are measured in 18 min. Further reducing the acquisition time could be achieved by working with a more sensitive photomultiplier and a DMD with a larger on-board memory. Finally, to obtain direct images of the sample, we used a $\times 20$ objective (Mitutoyo Plan Apo SL 20X/0.28) located on the other side of the sample, along with a 200 mm lens, a fluorescence filter (Chroma ET590/50m) and a complementary metal oxide semiconductor (CMOS) camera (Basler acA1300-200um). Direct images were then obtained by averaging measured images over random illumination patterns coming from the fiber.

ACKNOWLEDGMENTS

The authors thank M. Balland, A. Carron, A. Goetschy and S. Mezil for insightful discussions. This work was supported by the H2020 European Research Council (grant 681514-COHERENCE) and by a Marie Skłodowska Curie Individual Fellowship (grant 750420-DARWIN).

-
- [1] J. A. Frank, M.-J. Antonini, and P. Anikeeva, Next-generation interfaces for studying neural function, *Nat. Biotechnol.* **37**, 1013 (2019).
 - [2] A. W. Snyder and J. Love, *Optical Waveguide Theory* (Springer, 2012).
 - [3] R. N. Mahalati, R. Y. Gu, and J. M. Kahn, Resolution limits for imaging through multi-mode fiber, *Opt. Express* **21**, 1656 (2013).
 - [4] H. Cao, A. P. Mosk, and S. Rotter, Shaping the propagation of light in complex media, *Nat. Phys.* **18**, 994 (2022).

- [5] M. A. Bolshtyansky and B. Y. Zel'dovich, Transmission of the image signal with the use of a multimode fiber, *Opt. Commun.* **123**, 629 (1996).
- [6] T. Čižmár and K. Dholakia, Exploiting multimode waveguides for pure fibre-based imaging, *Nat. Commun.* **3**, 1027 (2012).
- [7] Y. Choi, C. Yoon, M. Kim, T. D. Yang, C. Fang-Yen, R. R. Dasari, K. J. Lee, and W. Choi, Scanner-Free and Wide-Field Endoscopic Imaging by Using a Single Multimode Optical Fiber, *Phys. Rev. Lett.* **109**, 203901 (2012).
- [8] I. N. Papadopoulos, S. Farahi, C. Moser, and D. Psaltis, High-resolution, lensless endoscope based on digital scanning through a multimode optical fiber, *Biomed. Opt. Express* **4**, 260 (2013).
- [9] A. M. Caravaca-Aguirre and R. Piestun, Single multimode fiber endoscope, *Opt. Express* **25**, 1656 (2017).
- [10] L. V. Amitonova and J. F. de Boer, Endo-microscopy beyond the Abbe and Nyquist limits, *Light Sci. Appl.* **9**, 81 (2020).
- [11] M. W. Matthès, Y. Bromberg, J. de Rosny, and S. M. Popoff, Learning and Avoiding Disorder in Multimode Fibers, *Phys. Rev. X* **11**, 021060 (2021).
- [12] M. Plöschner, T. Tyc, and T. Čižmár, Seeing through chaos in multimode fibres, *Nat. Photonics* **9**, 529 (2015).
- [13] D. E. Boonzajer Flaes, J. Stopka, S. Turtaev, J. F. de Boer, T. Tyc, and T. Čižmár, Robustness of Light-Transport Processes to Bending Deformations in Graded-Index Multimode Waveguides, *Phys. Rev. Lett.* **120**, 233901 (2018).
- [14] J. Bertolotti, E. G. van Putten, C. Blum, A. Lagendijk, W. L. Vos, and A. P. Mosk, Non-invasive imaging through opaque scattering layers, *Nature* **491**, 232 (2012).
- [15] O. Katz, P. Heidmann, M. Fink, and S. Gigan, Non-invasive single-shot imaging through scattering layers and around corners via speckle correlations, *Nat. Photonics* **8**, 784 (2014).
- [16] O. Salhov, G. Weinberg, and O. Katz, Depth-resolved speckle-correlations imaging through scattering layers via coherence gating, *Opt. Lett.* **43**, 5528 (2018).
- [17] D. Wang, S. K. Sahoo, X. Zhu, G. Adamo, and C. Dang, Non-invasive super-resolution imaging through dynamic scattering media, *Nat. Commun.* **12**, 3150 (2021).
- [18] L. Zhu, F. Soldevila, C. Moretti, A. d'Arco, A. Boniface, X. Shao, H. B. de Aguiar, and S. Gigan, Large field-of-view non-invasive imaging through scattering layers using fluctuating random illumination, *Nat. Commun.* **13**, 1447 (2022).
- [19] S. Feng, C. Kane, P. A. Lee, and A. D. Stone, Correlations and Fluctuations of Coherent Wave Transmission through Disordered Media, *Phys. Rev. Lett.* **61**, 834 (1988).
- [20] I. Freund, M. Rosenbluh, and S. Feng, Memory Effects in Propagation of Optical Waves through Disordered Media, *Phys. Rev. Lett.* **61**, 2328 (1988).
- [21] S. Schott, J. Bertolotti, J.-F. Léger, L. Bourdieu, and S. Gigan, Characterization of the angular memory effect of scattered light in biological tissues, *Opt. Express* **23**, 13505 (2015).
- [22] B. Judkewitz, R. Horstmeyer, I. M. Vellekoop, I. N. Papadopoulos, and C. Yang, Translation correlations in anisotropically scattering media, *Nat. Phys.* **11**, 684 (2015).
- [23] G. Osnabrugge, R. Horstmeyer, I. N. Papadopoulos, B. Judkewitz, and I. M. Vellekoop, Generalized optical memory effect, *Optica* **4**, 886 (2017).
- [24] H. Yilmaz, C. W. Hsu, A. Goetschy, S. Bittner, S. Rotter, A. Yamilov, and H. Cao, Angular Memory Effect of Transmission Eigenchannels, *Phys. Rev. Lett.* **123**, 203901 (2019).
- [25] L. V. Amitonova, A. P. Mosk, and P. W. H. Pinkse, Rotational memory effect of a multimode fiber, *Opt. Express* **23**, 20569 (2015).
- [26] W. Xiong, C. W. Hsu, and H. Cao, Long-range spatio-temporal correlations in multimode fibers for pulse delivery, *Nat. Commun.* **10**, 2973 (2019).
- [27] S. Li, S. A. R. Horsley, T. Tyc, T. Čižmár, and D. B. Phillips, Memory effect assisted imaging through multimode optical fibres, *Nat. Commun.* **12**, 3751 (2021).
- [28] N. Borhani, E. Kakkava, C. Moser, and D. Psaltis, Learning to see through multimode fibers, *Optica* **5**, 960 (2018).
- [29] B. Rahmani, D. Loterie, G. Konstantinou, D. Psaltis, and C. Moser, Multimode optical fiber transmission with a deep learning network, *Light Sci. Appl.* **7**, 69 (2018).
- [30] P. Fan, T. Zhao, and L. Su, Deep learning the high variability and randomness inside multimode fibers, *Opt. Express* **27**, 20241 (2019).
- [31] S. Resisi, S. M. Popoff, and Y. Bromberg, Image Transmission Through a Dynamically Perturbed Multimode Fiber by Deep Learning, *Laser Photonics Rev.* **15**, 2000553 (2021).
- [32] E. R. Andresen, S. Sivankutty, V. Tsvirkun, G. Bouwmans, and H. Rigneault, Ultrathin endoscopes based on multicore fibers and adaptive optics: a status review and perspectives, *J. Biomed. Opt.* **21**, 121506 (2016).
- [33] T. Yeminy and O. Katz, Guidestar-free image-guided wavefront shaping, *Sci. Adv.* **7**, eabf5364 (2021).
- [34] R. Kuschmierz, E. Scharf, D. F. Ortegón-González, T. Glosemeyer, and J. W. Czarske, Ultra-thin 3D lensless fiber endoscopy using diffractive optical elements and deep neural networks, *Light: Adv. Manuf.* **2**, 415 (2021).
- [35] M. C. Velsink, Z. Lyu, P. W. H. Pinkse, and L. V. Amitonova, Comparison of round- and square-core fibers for sensing, imaging, and spectroscopy, *Opt. Express* **29**, 6523 (2021).
- [36] A. M. Caravaca-Aguirre, A. Carron, S. Mezil, I. Wang, and E. Bossy, Optical memory effect in square multimode fibers, *Opt. Lett.* **46**, 4924 (2021).
- [37] J. R. Fienup, Reconstruction of an object from the modulus of its Fourier transform, *Opt. Lett.* **3**, 27 (1978).
- [38] Y. Shechtman, Y. C. Eldar, O. Cohen, H. N. Chapman, J. Miao, and M. Segev, Phase Retrieval with Application to Optical Imaging: A contemporary overview, *IEEE Signal Process. Mag.* **32**, 87 (2015).
- [39] S. Kirkpatrick, C. D. Gelatt, and M. P. Vecchi, Optimization by Simulated Annealing, *Science* **220**, 671 (1983).
- [40] S. Weisenburger and A. Vaziri, A guide to emerging technologies for large-scale and whole brain optical imaging of neuronal activity, *Annu. Rev. Neurosci.* **41**, 431 (2018).
- [41] S. Turtaev, I. T. Leite, T. Altweig-Boussac, J. M. P. Pakan, N. L. Rochefort, and T. Čižmár, High-fidelity multimode fibre-based endoscopy for deep brain *in vivo* imaging, *Light Sci. Appl.* **7**, 92 (2018).
- [42] Y. C. Eldar and G. Kutyniok, *Compressed sensing: theory and applications* (Cambridge University Press, 2012).
- [43] G. Barbastathis, A. Ozcan, and G. Situ, On the use of deep learning for computational imaging, *Optica* **6**, 921 (2019).

- [44] L. V. Wang and J. Yao, A practical guide to photoacoustic tomography in the life sciences, *Nat. Methods* **13**, 627 (2016).
- [45] A. M. Caravaca-Aguirre, S. Singh, S. Labouesse, M. V. Baratta, R. Piestun, and E. Bossy, Hybrid photoacoustic-fluorescence microendoscopy through a multimode fiber using speckle illumination, *APL Photonics* **4**, 096103 (2019).
- [46] J. Zhou and J. V. Jokerst, Photoacoustic imaging with fiber optic technology: A review, *Photoacoustics* **20**, 100211 (2020).
- [47] P. Campagnola and C.-Y. Dong, Second harmonic generation microscopy: principles and applications to disease diagnosis, *Laser Photonics Rev.* **5**, 13 (2011).
- [48] A. Cifuentes, T. Pikálek, P. Ondráčková, R. Amezcu-Correia, J. E. Antonio-Lopez, T. Čižmár, and J. Trägårdh, Polarization-resolved second-harmonic generation imaging through a multimode fiber, *Optica* **8**, 1065 (2021).
- [49] W.-H. Lee, Binary Synthetic Holograms, *Appl. Opt.* **13**, 1677 (1974).

Speckle-correlation imaging through a kaleidoscopic multimode fiber

Supplementary information

Dorian Bouchet,¹ Antonio M. Caravaca-Aguirre,¹ Philippe Moreau,¹ Irène Wang,¹ and Emmanuel Bossy¹

¹ Université Grenoble Alpes, CNRS, LIPhy, 38000 Grenoble, France

S1. SCHEMATIC REPRESENTATION OF THE OPTICAL SETUP

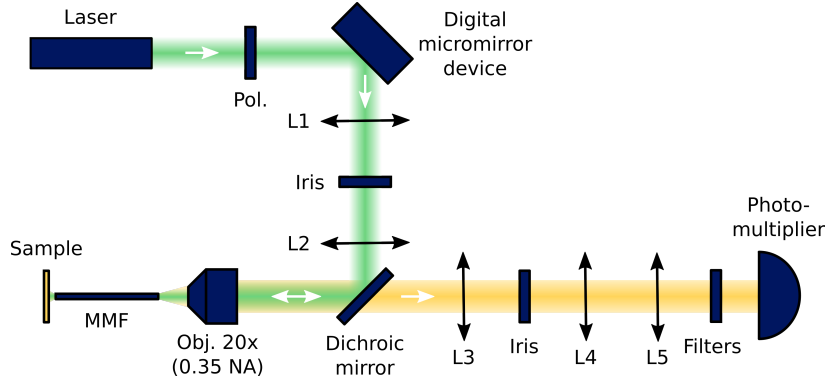


FIG. S1. Optical setup. Speckle patterns are generated using a digital micromirror device (DMD) and translated at the input of a square-core multimode fiber. A sample composed of fluorescent beads is placed at the output of the fiber. Fluorescence collected through the fiber passes a dichroic mirror and is detected by a single-channel photomultiplier. MMF: multimode fiber; Pol, linear polarizer; Obj, objective; NA, numerical aperture; L1 to L5, lenses with focal length 300 mm (L1), 150 mm (L2), 200 mm (L3), 100 mm (L4) and 150 mm (L5).

S2. CALCULATION OF THE SIGNAL AUTOCORRELATION: GENERAL EXPRESSION

The density distribution of fluorescent emitters $O(\mathbf{r}_b)$ is related to the measured fluorescence signal $S(\mathbf{r}_a)$ by the following relation:

$$S(\mathbf{r}_a) = \int O(\mathbf{r}_b) I(\mathbf{r}_a, \mathbf{r}_b) d\mathbf{r}_b, \quad (\text{S1})$$

where $I(\mathbf{r}_a, \mathbf{r}_b)$ is the excitation intensity transmitted at a position \mathbf{r}_b at the fiber output for a translation \mathbf{r}_a of the speckle pattern at the fiber input. The statistical autocorrelation function of the fluorescence signal is defined as follows:

$$C_S(\mathbf{r}_a, \mathbf{r}'_a) = \frac{\langle S(\mathbf{r}_a)S(\mathbf{r}'_a) \rangle - \langle S(\mathbf{r}_a) \rangle \langle S(\mathbf{r}'_a) \rangle}{\sqrt{\langle S(\mathbf{r}_a)^2 \rangle - \langle S(\mathbf{r}_a) \rangle^2} \times \sqrt{\langle S(\mathbf{r}'_a)^2 \rangle - \langle S(\mathbf{r}'_a) \rangle^2}}, \quad (\text{S2})$$

where $\langle \dots \rangle$ represents the average over different realizations of the speckle pattern at the fiber input. We also define the contrast of the signal $K(\mathbf{r}_a)$ as follows:

$$K(\mathbf{r}_a) = \frac{\sqrt{\langle S(\mathbf{r}_a)^2 \rangle - \langle S(\mathbf{r}_a) \rangle^2}}{\langle S(\mathbf{r}_a) \rangle}. \quad (\text{S3})$$

Using this definition, Eq. (S2) reads

$$C_S(\mathbf{r}_a, \mathbf{r}'_a) = \frac{\langle S(\mathbf{r}_a)S(\mathbf{r}'_a) \rangle - \langle S(\mathbf{r}_a) \rangle \langle S(\mathbf{r}'_a) \rangle}{K(\mathbf{r}_a)\langle S(\mathbf{r}_a) \rangle \times K(\mathbf{r}'_a)\langle S(\mathbf{r}'_a) \rangle}. \quad (\text{S4})$$

Using Eq. (S1), the average fluorescence signal can be expressed as follows:

$$\langle S(\mathbf{r}_a) \rangle = \langle I(\mathbf{r}_a, \mathbf{r}_b) \rangle \int O(\mathbf{r}_b) d\mathbf{r}_b. \quad (\text{S5})$$

Moreover, the correlator $\langle S(\mathbf{r}_a)S(\mathbf{r}'_a) \rangle$ is given by

$$\langle S(\mathbf{r}_a)S(\mathbf{r}'_a) \rangle = \iint O(\mathbf{r}_b)O(\mathbf{r}'_b)\langle I(\mathbf{r}_a, \mathbf{r}_b)I(\mathbf{r}'_a, \mathbf{r}'_b) \rangle d\mathbf{r}_b d\mathbf{r}'_b. \quad (\text{S6})$$

Inserting Eqs. (S5) and (S6) into Eq. (S2) yields

$$C_S(\mathbf{r}_a, \mathbf{r}'_a) = \frac{\iint O(\mathbf{r}_b)O(\mathbf{r}'_b)[\langle I(\mathbf{r}_a, \mathbf{r}_b)I(\mathbf{r}'_a, \mathbf{r}'_b) \rangle - \langle I(\mathbf{r}_a, \mathbf{r}_b) \rangle \langle I(\mathbf{r}'_a, \mathbf{r}'_b) \rangle] d\mathbf{r}_b d\mathbf{r}'_b}{K(\mathbf{r}_a)K(\mathbf{r}'_a) [\int O(\mathbf{r}_b) d\mathbf{r}_b]^2 \langle I(\mathbf{r}_a, \mathbf{r}_b) \rangle \langle I(\mathbf{r}'_a, \mathbf{r}'_b) \rangle}. \quad (\text{S7})$$

In this expression, we can recognize the definition of the statistical correlation function of the intensity:

$$C_I(\mathbf{r}_a, \mathbf{r}_b, \mathbf{r}'_a, \mathbf{r}'_b) = \frac{\langle I(\mathbf{r}_a, \mathbf{r}_b)I(\mathbf{r}'_a, \mathbf{r}'_b) \rangle - \langle I(\mathbf{r}_a, \mathbf{r}_b) \rangle \langle I(\mathbf{r}'_a, \mathbf{r}'_b) \rangle}{\langle I(\mathbf{r}_a, \mathbf{r}_b) \rangle \langle I(\mathbf{r}'_a, \mathbf{r}'_b) \rangle}. \quad (\text{S8})$$

Note that this correlation function is normalized: the speckle is assumed to be fully developed, so that $\langle I(\mathbf{r}_a, \mathbf{r}_b) \rangle = \sqrt{\langle I(\mathbf{r}_a)^2 \rangle - \langle I(\mathbf{r}_a) \rangle^2}$. Inserting Eq. (S8) into Eq. (S7) yields

$$C_S(\mathbf{r}_a, \mathbf{r}'_a) = \frac{\iint O(\mathbf{r}_b)O(\mathbf{r}'_b)C_I(\mathbf{r}_a, \mathbf{r}_b, \mathbf{r}'_a, \mathbf{r}'_b) d\mathbf{r}_b d\mathbf{r}'_b}{K(\mathbf{r}_a)K(\mathbf{r}'_a) [\int O(\mathbf{r}_b) d\mathbf{r}_b]^2}. \quad (\text{S9})$$

Shift-shift memory effects [1] (including the translational memory effect observed in square-core fibers) are described by an intensity correlation function $C_I(\mathbf{r}_a, \mathbf{r}_b, \mathbf{r}'_a, \mathbf{r}'_b) = C_I(\Delta\mathbf{r}_a, \Delta\mathbf{r}_b)$, where $\Delta\mathbf{r}_a = \mathbf{r}'_a - \mathbf{r}_a$ and $\Delta\mathbf{r}_b = \mathbf{r}'_b - \mathbf{r}_b$. In addition, $\langle I(\mathbf{r}_a, \mathbf{r}_b) \rangle$ and $\langle I(\mathbf{r}_a, \mathbf{r}_b)^2 \rangle$ are independent of \mathbf{r}_a and \mathbf{r}_b , implying that the signal contrast K is also independent of \mathbf{r}_a . This yields

$$C_S(\Delta\mathbf{r}_a) = \frac{\iint O(\mathbf{r}_b)O(\mathbf{r}_b + \Delta\mathbf{r}_b)C_I(\Delta\mathbf{r}_a, \Delta\mathbf{r}_b) d\mathbf{r}_b d\Delta\mathbf{r}_b}{K^2 [\int O(\mathbf{r}_b) d\mathbf{r}_b]^2}. \quad (\text{S10})$$

In this expression, we can recognize the spatial autocorrelation function of the object:

$$C_O(\Delta\mathbf{r}_b) = \frac{\int O(\mathbf{r}_b)O(\mathbf{r}_b + \Delta\mathbf{r}_b) d\mathbf{r}_b}{[\int O(\mathbf{r}_b) d\mathbf{r}_b]^2}. \quad (\text{S11})$$

Inserting Eq. (S11) into Eq. (S10) yields

$$C_S(\Delta\mathbf{r}_a) = K^{-2} \int C_O(\Delta\mathbf{r}_b)C_I(\Delta\mathbf{r}_a, \Delta\mathbf{r}_b) d\Delta\mathbf{r}_b. \quad (\text{S12})$$

This expression, given as Eq. (1) in the manuscript, relates the autocorrelation function of the fluorescence signal $C_S(\Delta\mathbf{r}_a)$, the object autocorrelation function $C_O(\Delta\mathbf{r}_b)$ and the intensity correlation function of the coherent excitation field $C_I(\Delta\mathbf{r}_a, \Delta\mathbf{r}_b)$.

S3. CALCULATION OF THE SIGNAL AUTOCORRELATION: LIMITING CASE

For an ideal model of square-core fibers with an infinite-range memory effect, the intensity correlation function $C_I(\Delta\mathbf{r}_a, \Delta\mathbf{r}_b)$ is given by [2]

$$C_I(\Delta\mathbf{r}_a, \Delta\mathbf{r}_b) = \frac{1}{16} \sum_{j=1}^4 \sum_{k=1}^4 C_j(\Delta\mathbf{r}_a, \Delta\mathbf{r}_b)C_k(\Delta\mathbf{r}_a, \Delta\mathbf{r}_b). \quad (\text{S13})$$

In this expression, the terms C_j are field correlation functions defined as follows:

$$C_j(\Delta\mathbf{r}_a, \Delta\mathbf{r}_b) = \frac{2J_1(k_0 \text{NA} \sqrt{(\Delta x_b - \xi_{x,j}\Delta x_a)^2 + (\Delta y_b - \xi_{y,j}\Delta y_a)^2})}{k_0 \text{NA} \sqrt{(\Delta x_b - \xi_{x,j}\Delta x_a)^2 + (\Delta y_b - \xi_{y,j}\Delta y_a)^2}}, \quad (\text{S14})$$

where J_1 is the first-order Bessel function of the first kind, $k_0 = 2\pi/\lambda$ is the wavenumber, NA is the numerical aperture of the fiber, $\xi_{x,1} = \xi_{x,3} = \xi_{y,1} = \xi_{y,2} = 1$ and $\xi_{x,2} = \xi_{x,4} = \xi_{y,3} = \xi_{y,4} = -1$. Field correlation functions defined by Eq. (S14) are composed of a single peak. These functions constitute the building blocks of the intensity correlation function given by Eq. (S13), which is characterized by four peaks that translate with $\Delta\mathbf{r}_a$ and that coherently overlap by pair when $\Delta x_a = 0$ or $\Delta y_a = 0$.

Assuming that the correlation functions $C_j(\Delta\mathbf{r}_a, \Delta\mathbf{r}_b)$ are infinitely sharp (i.e. assuming that the size of the speckle grain is small as compared to the smallest features of the object), we can find approximate expressions for the product $C_j(\Delta\mathbf{r}_a, \Delta\mathbf{r}_b)C_k(\Delta\mathbf{r}_a, \Delta\mathbf{r}_b)$. When $\Delta x_a(\xi_{x,j} - \xi_{x,k}) = 0$ and $\Delta y_a(\xi_{y,j} - \xi_{y,k}) = 0$, we can write

$$C_j(\Delta\mathbf{r}_a, \Delta\mathbf{r}_b)C_k(\Delta\mathbf{r}_a, \Delta\mathbf{r}_b) = A\delta(\Delta x_b - \xi_{x,j}\Delta x_a)\delta(\Delta y_b - \xi_{y,j}\Delta y_a), \quad (\text{S15})$$

where δ denotes the Dirac delta function and $A = 4\pi/(k_0 \text{NA})^2$ is the area covered by a speckle grain. In contrast, when $\Delta x_a(\xi_{x,j} - \xi_{x,k}) \neq 0$ or $\Delta y_a(\xi_{y,j} - \xi_{y,k}) \neq 0$, we can write

$$C_j(\Delta\mathbf{r}_a, \Delta\mathbf{r}_b)C_k(\Delta\mathbf{r}_a, \Delta\mathbf{r}_b) = 0. \quad (\text{S16})$$

Using these approximations to calculate the intensity correlation function given by Eq. (S13), the signal autocorrelation expressed by Eq. (S12) can be simplified as follows:

- when $\Delta x_a \neq 0$ and $\Delta y_a \neq 0$, we have

$$C_S(\Delta\mathbf{r}_a) = \frac{A}{16K^2} [C_O(\Delta x_a, \Delta y_a) + C_O(-\Delta x_a, \Delta y_a) + C_O(\Delta x_a, -\Delta y_a) + C_O(-\Delta x_a, -\Delta y_a)]; \quad (\text{S17})$$

- when $\Delta x_a = 0$ and $\Delta y_a \neq 0$, we have

$$C_S(\Delta\mathbf{r}_a) = \frac{A}{4K^2} [C_O(\Delta x_a = 0, \Delta y_a) + C_O(\Delta x_a = 0, -\Delta y_a)]; \quad (\text{S18})$$

- when $\Delta x_a \neq 0$ and $\Delta y_a = 0$, we have

$$C_S(\Delta\mathbf{r}_a) = \frac{A}{4K^2} [C_O(\Delta x_a, \Delta y_a = 0) + C_O(-\Delta x_a, \Delta y_a = 0)]; \quad (\text{S19})$$

- when $\Delta x_a = 0$ and $\Delta y_a = 0$, we have

$$C_S(\Delta\mathbf{r}_a) = \frac{A}{K^2} C_O(\Delta x_a = 0, \Delta y_a = 0). \quad (\text{S20})$$

Since C_O is an even function, we can write $C_O(\Delta x_a, \Delta y_a) = C_O(-\Delta x_a, -\Delta y_a)$ and $C_O(\Delta x_a, -\Delta y_a) = C_O(-\Delta x_a, \Delta y_a)$. Defining $C_O^{\text{sym}}(\Delta\mathbf{r}_a) = [C_O(\Delta x_a, \Delta y_a) + C_O(\Delta x_a, -\Delta y_a)]/2$ as the symmetrized version of the object autocorrelation, we obtain

$$C_S(\Delta\mathbf{r}_a) = \frac{A}{K^2} \times \begin{cases} C_O^{\text{sym}}(\Delta\mathbf{r}_a)/4 & \text{if } \Delta x_a \neq 0 \text{ and } \Delta y_a \neq 0, \\ C_O^{\text{sym}}(\Delta\mathbf{r}_a)/2 & \text{if } \Delta x_a = 0 \text{ and } \Delta y_a \neq 0, \\ C_O^{\text{sym}}(\Delta\mathbf{r}_a)/2 & \text{if } \Delta x_a \neq 0 \text{ and } \Delta y_a = 0, \\ C_O^{\text{sym}}(\Delta\mathbf{r}_a) & \text{if } \Delta x_a = 0 \text{ and } \Delta y_a = 0. \end{cases} \quad (\text{S21})$$

This expression shows that, in the limiting case of an infinite-range memory effect with a speckle grain size approaching zero, the signal autocorrelation can be written as $C_S(\Delta\mathbf{r}_a) \propto w(\Delta\mathbf{r}_a)C_O^{\text{sym}}(\Delta\mathbf{r}_a)$, where w is a weight function that is equal to 1 if $\Delta x_a = 0$ and $\Delta y_a = 0$, to 1/2 if either $\Delta x_a = 0$ or $\Delta y_a = 0$, and to 1/4 otherwise.

S4. INHERENT AMBIGUITIES IN THE INVERSE PROBLEM

There are several possible solutions when trying to infer $O(\mathbf{r}_b)$ from $C_O^{\text{sym}}(\Delta\mathbf{r}_b)$. First, as in usual inverse autocorrelation problems, any shift of the object in the transverse plane leads to the same symmetrized autocorrelation function.

Moreover, since $C_O^{\text{sym}}(\Delta x_b, \Delta y_b) = C_O^{\text{sym}}(-\Delta x_b, \Delta y_b) = C_O^{\text{sym}}(\Delta x_b, -\Delta y_b) = C_O^{\text{sym}}(-\Delta x_b, -\Delta y_b)$, there exists four different objects that lead to the same symmetrized autocorrelation. These four objects are flipped versions of each other, as illustrated in Fig. S2. Note that a similar ambiguity also exists in usual inverse autocorrelation problems [3]: since $C_O(\Delta x_b, \Delta y_b) = C_O(-\Delta x_b, -\Delta y_b)$, there exists two different objects that lead to the same autocorrelation (the two objects represented in Fig. S2a and Fig. S2d).

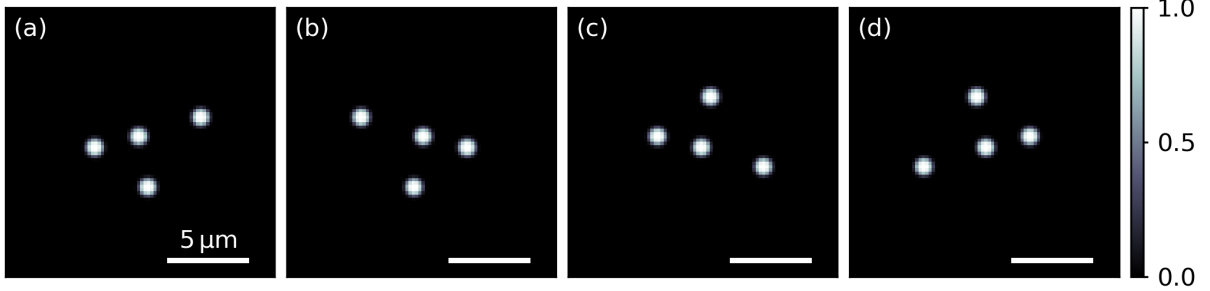


FIG. S2. Ambiguities in the inverse problem. These four different objects, that are flipped versions of each other, lead to the same symmetrized autocorrelation.

S5. INFLUENCE OF STATISTICAL FLUCTUATIONS ON THE RECONSTRUCTED IMAGES

In order to limit the influence of statistical fluctuations on the reconstructed images, it is necessary to average the measured signal autocorrelation over several realizations of input speckles. In the manuscript, we presented data obtained with $N_{\text{rep}} = 40,000$, yielding a signal correlation with no visible artifacts but requiring a significant acquisition time (4 hours in total). Nevertheless, information about the object is still available even for much lower numbers of realizations. To illustrate this, we compare in Fig. S3 signal autocorrelations and reconstructed images for different numbers of realizations of input speckles.

- For $N_{\text{rep}} = 200$ (acquisition time of 1 min 12 s), the shape of the objects is not faithfully reconstructed, but some distinctive features already appear on the signal autocorrelations (Fig. S3a,e,i).
- For $N_{\text{rep}} = 3,000$ (acquisition time of 18 min), the shape of the objects can already be recognized, but a few beads are slightly mislocalized. In this case, signal autocorrelations strongly resemble the theoretical predictions (Fig. S3d,h,l), even though artifacts can be observed on the edge of the autocorrelations—edges are more sensitive to statistical fluctuations, as they benefit from a weaker spatial averaging effect.
- For $N_{\text{rep}} = 40,000$ (acquisition time of 4 hours), no artifacts due to statistical fluctuations can be observed, and the position of the beads is correctly retrieved (Fig. S3c,g,k).

Note that objects with a large number of beads are typically more sensitive to statistical fluctuations, and it can happen that, even for a large number of realizations of input speckles, two different beads configurations lead to similar signal autocorrelations that are hard to separate, preventing us to image objects with large numbers of beads using the current reconstruction procedure.

S6. DETERMINATION OF THE NUMBER OF FLUORESCENT BEADS

In principle, the number of fluorescent beads could be determined directly from the measured signal autocorrelation. Nevertheless, a more robust strategy consists in analyzing the statistics of the measured signal. The voltage distribution associated with the fluorescence signal measured through the fiber is shown in Fig. S4 for the three objects shown in the manuscript (composed of 2, 3 and 4 beads, respectively). For comparison purposes, we also present the distribution obtained in the case of 0 and 1 bead. The average value of these distributions is proportional to the number of beads, with approximately 0.40 V for each bead. Experimentally, we observed average values of 0.87 V for the object composed of 2 beads, 1.17 V for the object composed of 3 beads and 1.60 V for the object composed of 4 beads, allowing us to easily infer the number of beads for these samples.

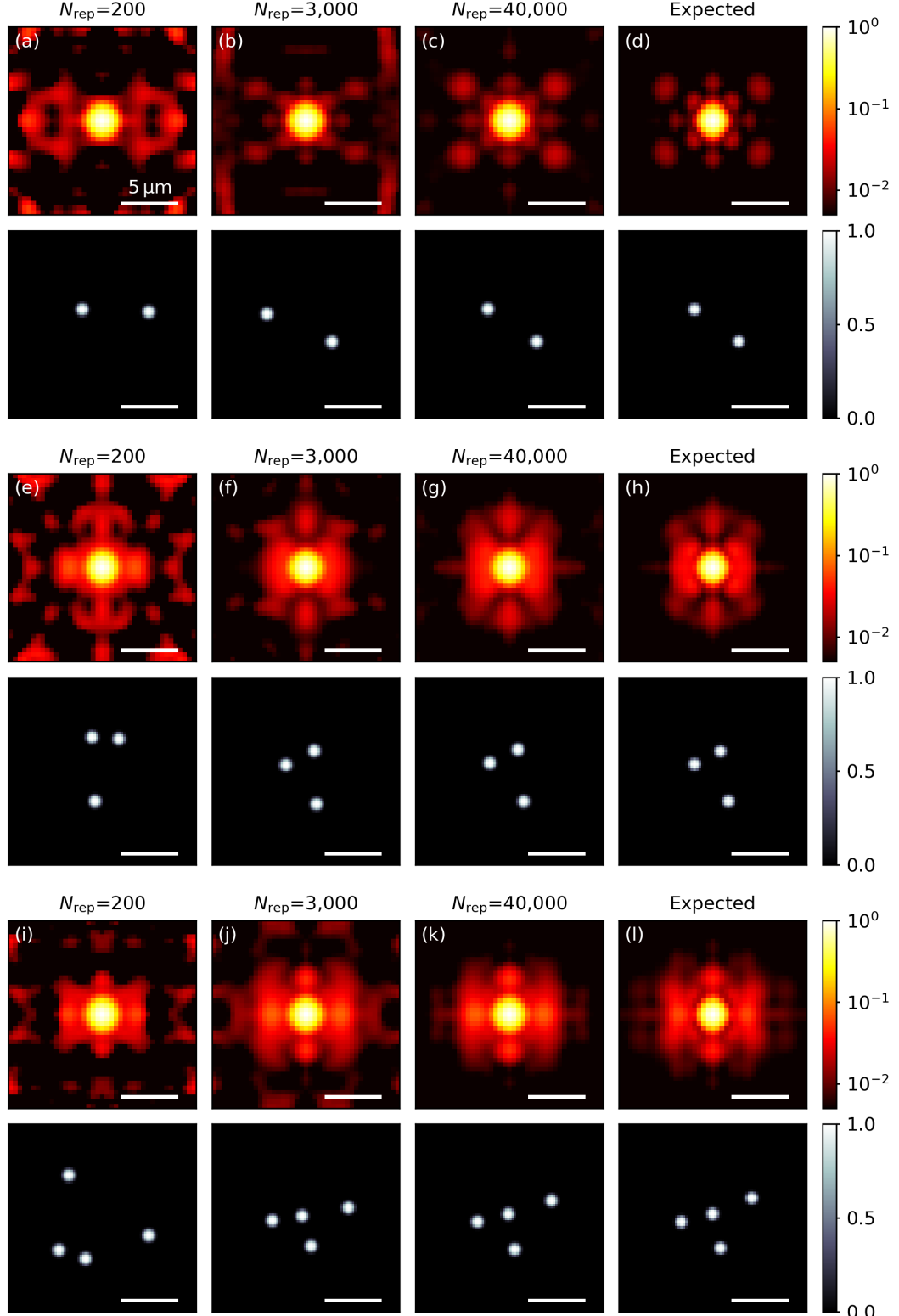


FIG. S3. Signal autocorrelations retrieved from experimental measurements and reconstructed images for different numbers of realizations of input speckles. (a-c) Signal autocorrelation (top) and reconstructed images (bottom) for the sample composed of two beads, for $N_{\text{rep}} = 200$ realizations (a), $N_{\text{rep}} = 3,000$ (b) and $N_{\text{rep}} = 40,000$ (c). (d) Theoretically-predicted signal autocorrelation (left) along with the true position of the beads (right). (d-h) Analogous to (a-d) for the object composed of three fluorescent beads. (i-l) Analogous to (a-d) for the object composed of four fluorescent beads.

Note that another strategy would consist in analyzing the contrast of the measured signals, defined as the ratio between the standard deviation and the average value of the fluorescence signal. In theory, the contrast is equal to $1/\sqrt{n}$ for n point-like fluorescent emitters [4]. Contrasts measured in our experiment do not reach this theoretical limit, which is expected as the size of the beads ($1.0\text{ }\mu\text{m}$ in diameter) is comparable to that of the speckle grain ($0.5\lambda/\text{NA} = 1.2\text{ }\mu\text{m}$). Nevertheless, observed contrasts do decrease with the number of beads (0.71 for 1 bead, 0.50 for 2 beads, 0.37 for 3 beads and 0.28 for 4 beads), which indicates that analyzing the contrast is also a possible strategy to determine the number of beads (using e.g. a suitable theoretical model).

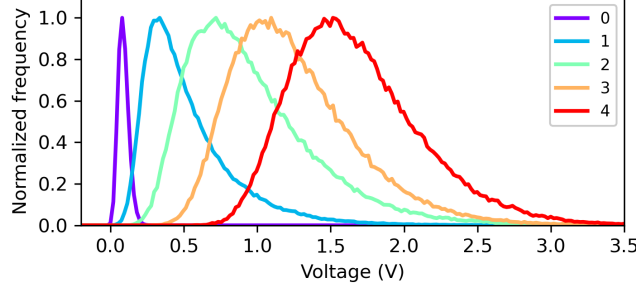


FIG. S4. Statistics of the measured fluorescence signal for different numbers of beads. Voltage distribution associated with the fluorescence signal measured through the fiber for a number of beads ranging from 0 to 4 . Both the average value and the contrast of these distributions can be used to determine the number of beads.

S7. DESCRIPTION OF THE RECONSTRUCTION PROCEDURE

Our reconstruction procedure is based on three essential features: the processing of the experimental data, the implementation of the theoretical model, and the optimization algorithm.

S7.1. Processing of the experimental data

The fluorescence signal is experimentally measured for $N_{\text{rep}} = 40,000$ realizations of input speckles. For each realization, we sequentially construct a 21×21 image by translating the input speckle pattern over an area of $8\text{ }\mu\text{m} \times 8\text{ }\mu\text{m}$ and by measuring the resulting intensity with the photomultiplier (Fig. S5a). This signal is known to be band-limited in the spatial domain due to the finite size of the speckle grain; thus, we apply a Gaussian spatial filter to the measured signal in order to reduce fluctuations arising from measurement noise (Fig. S5b). Due to the significant acquisition time, we also observed a slow decay of the average signal measured by the photomultiplier, which can be due to laser power fluctuations and to the slow photobleaching of the beads (Fig. S5c). Therefore, we fit a function based on cubic splines to the temporal dependence of the signal, and we use this function to compensate for this decay (Fig. S5d). The normalized signal autocorrelation function $C_S(\Delta\mathbf{r}_a)$ is then directly calculated from its definition [see Eq. (S2)], averaging over all possible spatial pairs and all realizations of input speckles. Finally, we take advantage of the known symmetry of the signal autocorrelation function and average the calculated signal autocorrelation with its left-right flipped version (or, equivalently, with its up-down flipped version), which further reduces the influence of statistical fluctuations. As a result, we obtain the signal correlation function estimated from experimental measurements, that we denote $C_S^{\text{meas}}(\Delta\mathbf{r}_a)$.

S7.2. Implementation of the theoretical model

In order to theoretically predict the signal autocorrelation from Eq. (S12), we must develop a model for the object function $O(\mathbf{r}_b)$. For this purpose, we model fluorescent beads as high-order Gaussian functions of exponent 2, with the same amplitude for all beads and a full width at half maximum equal to $1\text{ }\mu\text{m}$ (i.e. the known diameter of the beads). The object function $O(\mathbf{r}_b)$ is constructed by summing all contributions from the beads (see Fig. 2b of the manuscript),

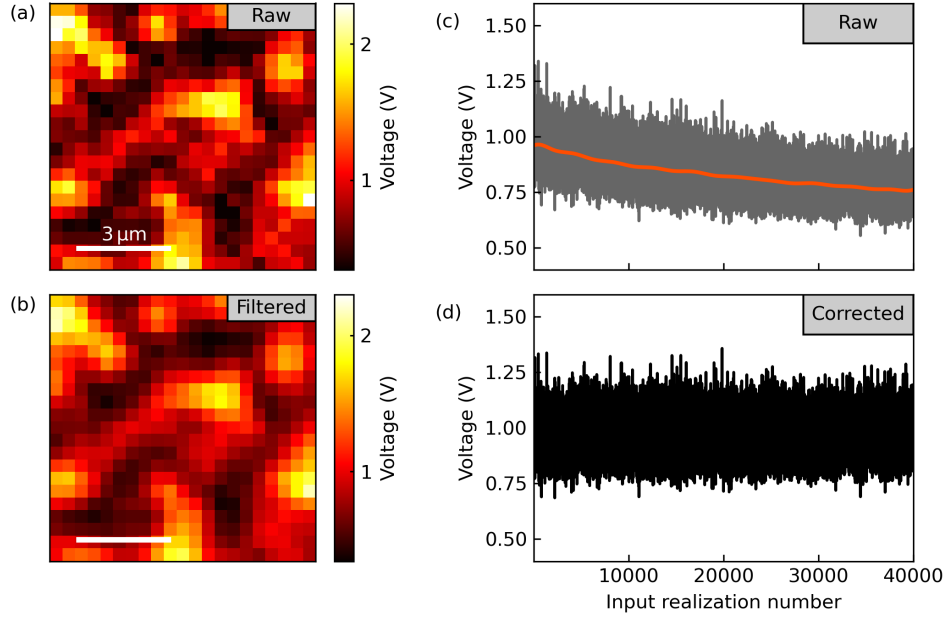


FIG. S5. Processing of measured experimental data. (a) Example of a raw fluorescence signal measured by the photomultiplier as a function of $\Delta\mathbf{r}_a$, shown here for the object composed of 2 beads. (b) Same signal as in (a) after being smoothed by a Gaussian spatial filter, that we used to reduce the influence of measurement noise. (c) Average signal measured by the photomultiplier as a function of the number of input speckle realizations (gray curve), along with a model function (orange curve) based on cubic splines. (d) Same signal as in (c) after being compensated for the observed decay.

and its spatial autocorrelation $C_O(\Delta\mathbf{r}_b)$ is numerically calculated from $O(\mathbf{r}_b)$ (see Fig. 2c of the manuscript). In addition to $C_O(\Delta\mathbf{r}_b)$, the theoretical expression of the signal autocorrelation also involves the intensity correlation function $C_I(\Delta\mathbf{r}_a, \Delta\mathbf{r}_b)$. While we could use the expression of $C_I(\Delta\mathbf{r}_a, \Delta\mathbf{r}_b)$ that was obtained based on an ideal model of square-core fibers [see Eqs. (S13) and (S14)], this would not take into account the limited range of the memory effect that we experimentally observed. For this reason, we estimate $C_I(\Delta\mathbf{r}_a, \Delta\mathbf{r}_b)$ from experimental measurements. To this end, we image the intensity of the coherent field at the fiber output using a $\times 20$ objective (Mitutoyo Plan Apo SL 20X/0.28) along with a 200 mm lens and a CMOS camera (Basler acA1300-200um). We generate 10,000 realizations of input speckles, we translate them with the DMD (\mathbf{r}_a covers a $8 \mu\text{m} \times 8 \mu\text{m}$ area), and we record the intensity measured by the camera (\mathbf{r}_b covers a $14.6 \mu\text{m} \times 14.6 \mu\text{m}$ area). The normalized intensity correlation function $C_I(\Delta\mathbf{r}_a, \Delta\mathbf{r}_b)$ is then directly calculated from its definition [see Eq. (S8)], averaging over all possible spatial pairs and all realizations of input speckles (see Fig. 2d-g of the manuscript). Finally, the signal autocorrelation is calculated from $C_O(\Delta\mathbf{r}_b)$ and $C_I(\Delta\mathbf{r}_a, \Delta\mathbf{r}_b)$ using Eq. (S12). As a result, we obtain the predicted signal correlation function (see Fig. 2i of the manuscript), that we denote $C_S^{\text{pred}}(\Delta\mathbf{r}_a)$.

S7.3. Optimization algorithm

Our reconstruction algorithm is based on the minimization of a loss function that compares theoretical predictions to measured data. As the signal correlation significantly decays with the distance $\Delta\mathbf{r}_a$, and since the positions of the beads are typically encoded into large values of $\Delta\mathbf{r}_a$, our loss function is defined using the logarithm of $C_S^{\text{meas}}(\Delta\mathbf{r}_a)$ and $C_S^{\text{pred}}(\Delta\mathbf{r}_a)$, which efficiently increases the contribution of the most useful parts of the signal correlation function. However, this strategy also tends to increase the contribution of artifacts that are due to statistical fluctuations. Thus, we define a threshold V_{\min} below which values of $C_S^{\text{meas}}(\Delta\mathbf{r}_a)$ are considered as artifacts and are not taken into account for the calculation of the loss function. In practice, we set this threshold to $V_{\min} = 5 \times 10^{-3}$ for all of our reconstructions; note that we also used this value as a lower limit for the colormaps used to represent the data (see Fig. 3 of the manuscript). Denoting $\tilde{C}_S^{\text{meas}}(\Delta\mathbf{r}_a)$ and $\tilde{C}_S^{\text{pred}}(\Delta\mathbf{r}_a)$ the functions $C_S^{\text{meas}}(\Delta\mathbf{r}_a)$ and $C_S^{\text{pred}}(\Delta\mathbf{r}_a)$ defined

on the restricted domain for which $C_S^{\text{meas}}(\Delta \mathbf{r}_a) \geq V_{\min}$, we use the following loss function:

$$L(\theta) = \left\| \log[\tilde{C}_S^{\text{meas}}(\Delta \mathbf{r}_a)] - \log[\tilde{C}_S^{\text{pred}}(\Delta \mathbf{r}_a, \theta)] \right\|^2 + R_{\text{fov}}(\theta) + R_{\text{dmin}}(\theta) + R_{\text{dmax}}(\theta), \quad (\text{S22})$$

where $\|\dots\|$ denotes the Euclidean distance (i.e. the L2 norm), $\theta = \{x_i, y_i\}_{i=1,\dots,n}$ denotes the positions of the n beads, and $R_{\text{fov}}(\theta)$, $R_{\text{dmin}}(\theta)$, and $R_{\text{dmax}}(\theta)$ denote three regularization terms. The first regularization term $R_{\text{fov}}(\theta)$ is an exponential potential that penalizes beads located outside the predefined field of view ($10 \mu\text{m} \times 10 \mu\text{m}$). The second regularization term $R_{\text{dmin}}(\theta)$ is an exponential potential function that penalizes beads that are too close to each other. In this way, we ensure that two beads cannot overlap. The third regularization term $R_{\text{dmax}}(\theta)$ is an exponential potential function that penalizes beads that are too far apart, based on the area for which $\tilde{C}_S^{\text{meas}}(\Delta \mathbf{r}_a)$ is defined. In this way, the distance between two beads is restricted to the area for which measured values of the signal correlation function are significant.

The cost function defined by Eq. (S22) is not convex, and must therefore be minimized using a global optimization strategy. To this end, we implemented an algorithm based on simulated annealing, which is an optimization algorithm inspired by statistical mechanics [5]. Starting with a random guess for the beads positions, the algorithm typically converges after $200 \times p$ iterations, where p is the number of parameters to be estimated (i.e. twice the number of beads since two coordinates must be estimated for each bead). To increase the probability that the global minimum was reached, we repeated this procedure for 20 different random initial guesses, and we kept the solution that yielded the lowest value of the loss function. The number of times that the algorithm converged to this optimal solution was 12/20 for the object composed of 2 beads, 16/20 for the object composed of 3 beads, and 3/20 for the object composed of 4 beads, which indicates that the inverse problem becomes more difficult to solve when increasing the number of beads. Note that the algorithm frequently reconstructs flipped versions of the objects, which is expected due to the known ambiguity in the inverse problem (see Supplementary Section S4). In the manuscript, reconstructed images were presented by selecting the version that best corresponds to the ground truth among the 4 possibilities.

- [1] G. Osnabrugge, R. Horstmeyer, I. N. Papadopoulos, B. Judkewitz, and I. M. Vellekoop, Generalized optical memory effect, *Optica* **4**, 886 (2017).
- [2] A. M. Caravaca-Aguirre, A. Carron, S. Mezil, I. Wang, and E. Bossy, Optical memory effect in square multimode fibers, *Opt. Lett.* **46**, 4924 (2021).
- [3] J. Bertolotti, E. G. van Putten, C. Blum, A. Lagendijk, W. L. Vos, and A. P. Mosk, Non-invasive imaging through opaque scattering layers, *Nature* **491**, 232 (2012).
- [4] O. Krichevsky and G. Bonnet, Fluorescence correlation spectroscopy: the technique and its applications, *Rep. Prog. Phys.* **65**, 251 (2002).
- [5] S. Kirkpatrick, C. D. Gelatt, and M. P. Vecchi, Optimization by Simulated Annealing, *Science* **220**, 671 (1983).